Design Rules for Dynamic-Template-Directed Crystallization of Conjugated Polymers

Journal:	*Molecular Systems Design & Engineering*
Manuscript ID	ME-ART-03-2019-000042.R1
Article Type:	Paper
Date Submitted by the Author:	27-Apr-2019
Complete List of Authors:	Mohammadi, Erfan; University of Illinois at Urbana-Champaign, Chemical & Biomolecular Engineering Qu, Ge; University of Illinois at Urbana-Champaign, Chemical & Biomolecular Engineering Kafle, Prapti; University of Illinois at Urbana-Champaign, Chemical & Biomolecular Engineering Jung, Seok-Heon; Inha University, Lee, Jin-Kyun; Inha University, Polymer Science & Engineering Diao, Ying; University of Illinois at Urbana-Champaign, Chemical & Biomolecular Engineering

DESIGN, SYSTEM, APPLICATION

Substrate surface properties are critical to determining the electronic properties of conjugated polymer (CP) thin films deposited atop during solution coating. Thus, it is necessary to better understand the role of substrate-ink interfacial properties in multiscale assembly and rationally engineer the surface characteristics accordingly. Herein, we lay out a general design rule for dynamic-template-directed crystallization of CPs that enable fabricating highly aligned and crystalline thin films over large area. By directly quantifying the enthalpy of polymer adsorption to the templates we demonstrate that both template dynamics and chemistry drastically modulate the interactions between template and CP. Stronger template-CP interactions facilitate nucleation and expedite the subsequent polymer crystallization process. Resultantly, templates with the highest enthalpy of absorption exhibit superior solid-state characteristics including higher molecular order, domain size and crystallinity as well as improved charge transport mobility. These findings provide fundamental insights on the importance substrate-polymer interactions during solution printing of CP thin films. Our developed design rules have broad implications beyond printed electronics given the critical role of interfaces in guiding assembly of various functional materials.

Design Rules for Dynamic-Template-Directed Crystallization of Conjugated Polymers

Erfan Mohammadi[1#], Ge Qu, Prapti Kafle, Seok-Heon Jung[2], Jin-Kyun Lee[2], Ying Diao[1*]

[1]*Department of Chemical and Biomolecular Engineering, University of Illinois at Urbana−Champaign, 600 South Mathews Avenue, Urbana, Illinois 61801, United States.*

[2]*Department of Polymer Science & Engineering, Inha University, Incheon 402-751, South Korea.*

ABSTRACT

The multiscale morphology and device performance of printed semiconducting polymers are highly sensitive to the substrate/ink interfacial properties during solution coating. There is an urgent need of general design rules correlating substrate properties and conjugated polymer (CP) morphology, which do not yet exist. Dynamic surfaces are particularly promising for templating highly crystalline and highly aligned conjugated polymer thin films shown in recent works. Herein, we implement the dynamic-templating method using a series of liquid-infused nanoporous substrates as a tool to study the impact of template reconfigurability and chemistry on multiscale morphology of conjugated polymer thin films, using a high performing donor-acceptor polymer (DPP-BTz) as a model compound. By quantifying enthalpy of adsorption, we demonstrate that the strength of template-CP interactions directly measures the effectiveness of dynamic surfaces in promoting conjugated polymer crystallization and alignment. We further show that enthalpy of interactions increases by enhancing template dynamics and are sensitively modulated by template chemistry. Specifically, increasing template-CP interactions leads to larger domain size and higher degree of crystallinity in templated conjugated polymer thin films prepared by meniscus-guided solution coating. This observation validates our hypothesis that dynamic templates function by promoting nucleation of conjugated polymers. We also demonstrate that such dynamic-template-dependent morphology is independent of coating speed. Notably, the enhanced morphological properties modulate the charge carrier mobility in field-effect transistors (FETs) over an order of magnitude reaching hole mobility of 2.8 $cm^2V^{-1}s^{-1}$. This work is a significant step towards establishing general guidelines on how substrate-ink interfacial properties influence morphology and performance of solution coated CP thin films.

DESIGN, SYSTEM, APPLICATION

Substrate surface properties are critical to determining the electronic properties of conjugated polymer (CP) thin films deposited atop during solution coating. Thus, it is necessary to better understand the role of substrate-ink interfacial properties in multiscale assembly and rationally engineer the surface characteristics accordingly. Herein, we lay out a general design rule for dynamic-template-directed crystallization of CPs that enable fabricating highly aligned and crystalline thin films over large area. By directly quantifying the enthalpy of polymer adsorption to the templates, we demonstrate that both template dynamics and chemistry drastically modulate the interactions between template and CP. Stronger template-CP interactions facilitate nucleation and expedite the subsequent polymer crystallization process. Resultantly, templates with the highest enthalpy of absorption exhibit superior solid-state characteristics including higher molecular order, domain size and crystallinity as well as improved charge transport mobility. These findings provide fundamental insights on the importance substrate-polymer interactions during solution printing of CP thin films. Our developed design rules have broad implications beyond printed electronics given the critical role of interfaces in guiding assembly of various functional materials.

INTRODUCTION

Semiconducting polymers demonstrate great potential for fabricating next generation of flexible electronics including transistors[1-2], solar cells[3-4], displays[5] and sensors[6-7]. The main advantage of conjugated polymers (CPs) is their solution-processability and low-cost large-area manufacturing. Electronic properties of solution-coated CP thin films are highly sensitive to morphological properties from molecular to device scale[8-10]. However, it is challenging to control CP multiscale assembly during non-equilibrium high-throughput solution coating. Traditionally, surface-induced crystallization facilitated by heterogenous nucleation is implemented as an effective strategy to control polymer nucleation and growth[11-12]. In particular, substrate interfacial properties play a critical role in guiding crystallization of solution-coated CPs[13-14] and it has been suggested that thin films often nucleate from the substrate-ink interface[15-17].

Surface topology and chemistry are the most studied parameters that influence thin film multiscale assembly during solution coating[13]. Modulating surface nanostructure[18] and roughness[19-20] influence solution wetting and/or evaporation behavior which alters crystalline domain size and ordering. On the other hand, surface chemistry primarily impacts CP crystallization via substrate-solvent and substrate-CP interactions, which further dictate the wetting and evaporation behavior. As an example, out-of-plane molecular orientation of poly(3-hexylthiophene) (P3HT) crystallites can be controlled effectively via substrate chemistry[21-22]. It has been suggested that strong interactions between P3HT backbone and substrate aliphatic or aromatic functional groups lead to “face-on” stacking. While polar surfaces induce dominantly “edge-on” orientation. Several investigations reported on improving in-plane molecular ordering of donor-acceptor (D-A) CP thin films using surface functionalizations[23-24]. Recently, we studied

the interplay between the substrate surface energy (γ_{SV}) and diketopyrrolopyrrole (DPP)-based CP multiscale crystallization[23]. We found that as γ_{SV} decreased from 67 to 20 mN.m^{-1} via surface treatment, in-plane alignment and relative degree of crystallinity systematically increased. We further developed a generic free energy model for heterogeneous nucleation suggesting that decreased nucleation energy barrier of lower γ_{SV} is responsible for enhanced crystallization. This trend was validated by Lee et al. wherein they obtained higher alignment and larger crystalline domains of solution-coated DPP-based CPs on substrates with lower γ_{SV}[24].

In addition to surface topology and chemistry, the important role of substrate dynamics is increasingly recognized, but remains under-explored. Marks et al. observed that the grain size of pentacene film can be controlled by polymer dielectric viscoelastic properties during vapor deposition[25]. They found that at high temperatures, surpassing the surface glass transition temperature ($T_{g,s}$), highly mobile polymer chains significantly increased pentacene nucleation density and disrupted formation of large crystalline grains. However, on rigid substrates grains became larger with increasing temperature. In a series of papers, floating film transfer (FFT) method was implemented to attain alignment in CP thin films by spreading the solution on passive liquid templates such as hydrogen-bonded and ionic liquid[26-29]. Typically, in these works the polymer is annealed to high temperatures (up to transition temperature for liquid crystalline polymers). Authors proposed that highly mobile free surface of liquid substrates facilitated rearrangement of polymer chains into a more ordered structure. However, such mechanism has not been validated and it remains unclear how substrate dynamics and chemistry influence the assembly and reorganization of CP. Recently, we introduced the dynamic templating method unveiling the essential role of surface reconfigurability and CP-substrate interactions in the assembly process[30], which is fundamentally different from FFT. We proposed that interactions

between a dynamic template and CPs can be promoted by reconfigurable surface exposing its favorable interacting sites. This enhanced interaction lowers the polymer nucleation barrier and expedite crystallization by adsorbing CP to the dynamic template interface. Resultantly, solution-coated CP thin films exhibited exceptional degrees of alignment and crystallinity not attainable using any known rigid (static) substrate.

In this work, we further investigate the critical role of template interactions with CP to derive design rules for dynamic-template-directed assembly during solution coating. To achieve this goal, we implement 5 different liquid templates of varying dynamics and chemistry including hydrogen-bonded and ionic liquids. DPP-BTz is used as a high-performance CP to evaluate the templating effect during meniscus-guided solution coating. The enthalpy of adsorption of DPP-BTz from solution onto dynamic template is directly measured using isothermal titration calorimetry (ITC). Our results demonstrate that both template dynamics and chemistry are essential for favorable interaction with the CP. To study the interplay between the substrate properties and thin film multiscale morphology, we perform comprehensive characterizations combining atomic force microscopy (AFM), cross-polarized optical microscopy (C-POM), UV-vis spectroscopy (UV-Vis) and grazing incidence X-ray diffraction (GIXD). Our results show that the polymer multiscale morphology is drastically modified by increasing template-CP interactions regardless of coating speed and final film thickness. Enhancing surface reconfigurability of hydrogen-bonded liquids leads to improved molecular order and relative degree of crystallinity. The highest molecular order, domain size and crystallinity are observed from IL-templated films that exhibit the highest enthalpy of absorption. The resultant charge transport mobility reaches 2.8 $cm^2V^{-1}s^{-1}$. Our findings provide rational guidelines for designing substrate-ink interfaces during large-scale solution-coating.

RESULTS AND DISCUSSION

Dynamic template design for polymer thin film fabrication. We employ a diketopyrrolopyrrole based D-A polymer, DPP-BTz, as a model semi-crystalline conjugated polymer (CP) given its high performance[31-32]. DPP-BTz films are fabricated from chloroform solution via a meniscus-guided coating (MGC) technique which mimics the physics of high-throughput roll-to-roll printers[23, 30, 33] (Figure 1) (see the Experimental section for MGC details). We choose two groups of liquid templates to obtain insight into the role of substrate dynamics and chemistry during solution coating. The first group includes two hydrogen-bonded liquids with comparable chemistry and drastically different dynamics (evaluated later): ethylene glycol (EG) and glycerol (GLY). The second group contains a series of ILs with different chemistry and comparable dynamics to EG. ILs are comprised of a bis(trifluoromethanesulfonyl)imide (TFSI) anion paired with three different cations of the families of ammonium (N4111), pyrrolidinium (PYR) and imidazolium (BMIM) with comparable alkyl chains. The chemical structures of the investigated templates are shown in Figure 1. Both hydrogen-bonded liquids and ILs can potentially interact strongly with the D-A polymer conjugated backbone through dipole-π or ion-π forces. We construct dynamic templates by infiltrating liquids in nanoporous anodized aluminum oxide (AAO) membrane supported by glass substrates. High capillary force induced by AAO nanopores ensures template compatibility with MGC and presence of a liquid-wetting layer to direct polymer crystallization[30]. We confirmed experimentally that all templates are practically immiscible with the CP solution in the short time frame of coating.

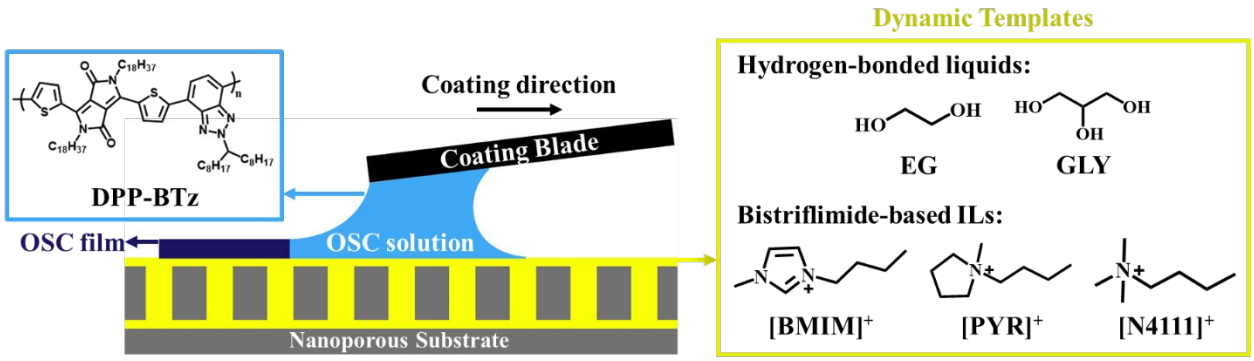

Figure 1. Schematic of meniscus-guided coating of DPP-BTz films on a series of dynamics templates. Dynamic templates are fabricated from infiltrating various liquids in AAO nanoporous membranes supported on glass substrates. The liquids include ethylene glycol (EG), glycerol (GLY), and 1-butyl-3-methylimidazolium bistriflimide ([BMIM][TFSI]), 1-butyl-1-methylpyrrolidinium bistriflimide ([PYR][TFSI]) and 1-butylammonium-1,1,1-trimethylammonium bistriflimide ([N4111][TFSI]). Molecular structures of DPP-BTz CP (blue) and dynamic templates (yellow) are shown in the inset. Schematic illustration of the MGC is not to scale.

Evaluating template-CP interactions for establishing design rules. For establishing template design rules, we hypothesize that the effect of the dynamic template directly scales with the extent of template-CP interactions, and that faster template dynamics acts by promoting template-CP interactions. We first compare template dynamics via orientational relaxation time (τ_{rot}) estimated from the Stokes-Einstein-Debye (SED) hydrodynamic theory[34-35]: $\tau_{rot} = \frac{3\eta V_{eff}\xi}{k_B T}$. In this equation η is viscosity, V_{eff} is the effective molecular volume and ξ is a factor which is a function of hydrodynamic boundary conditions (stick or slip). Table S1 summarizes the estimated τ_{rot} values relative to EG for all templates. This analysis reveals significantly slower dynamics of GLY compared to EG and ILs, which is not surprising given its high viscosity[36-37]. The estimated relative τ_{rot} agrees with the reported orientation relaxation time[38]. All three IL templates exhibit

comparable τ_{rot} on the same order as that of EG. The ultrafast dynamics of the selected ILs is demonstrated by previous experimental measurements (τ_{rot} <nanoseconds)[39-41].

We next quantify the interaction between DPP-BTz and various templates by isothermal titration calorimetry (ITC). ITC traditionally is used for directly measuring binding energetics in biological reactions[42-43] and recently its application has extended to macro- and nano-molecular systems[44-46]. However, this is the first time that this technique is implemented for measuring semiconducting polymers interaction with substrate. We choose single-injection ITC[47], shown in Figure 2a, to mimic a drop-casting experiment. During this experiment, CP solution is titrated onto the dynamic template and the released heat from the solution-template interaction is measured (ΔH_{soln}). Next, solvent titration enthalpy change (ΔH_{solv}) is measured in the exact same manner. Subtracting ΔH_{solv} from ΔH_{soln} would result in the net CP-template interaction enthalpy change (ΔH_{net}). Figure S1a-c present the raw heat rates and measured enthalpy changes for all templates. Figure 2b summarizes ΔH_{net}, suggesting favorable interaction with DPP-BTz (ΔH_{net}<0) for all hydrogen-bonded liquids and ILs. The ΔH_{net} from titrating polymer solution on EG is ~2 times higher than that of GLY despite comparable chemistry of the two templates. We attribute this to faster dynamics of EG that enable rapid surface reorganization to maximize its favorable interactions with DPP-BTz in the solution environment. ΔH_{net} values for ILs are significantly larger than EG. This is not surprising since IL cations can interact strongly with the conjugated polymer backbone via electrostatic forces and ion-π interactions proved by molecular dynamic simulations and ^{1}H NMR measurements[30]. Within the IL series, BMIM exhibit the strongest affinity to DPP-BTz with ~2 times higher ΔH_{net} compared to N4111 and PYR.

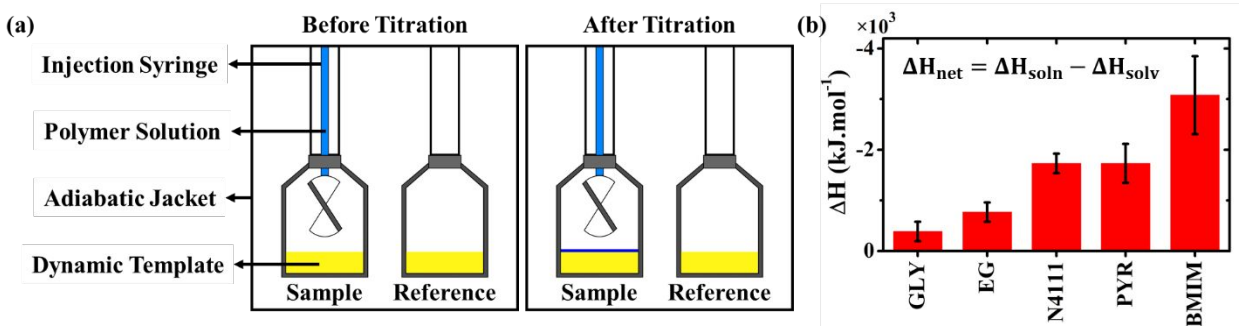

Figure 2. Quantify the interaction between DPP-BTz and dynamic templates using isothermal titration calorimetry (ITC). (a) Schematic illustration of sample and reference cells before and after titrating the DPP-BTz solution on the dynamic templates. The strength of interaction is proportional to the net heat released during the titration. (b) Enthalpy of interaction between DPP-BTz and various templates calculated from the difference between the heat released during the titration of polymer solution and the neat solvent.

Conjugated polymer multiscale morphology characterizations. DPP-BTz films are fabricated via MGC over a wide range of coating speeds (v) spanning from 0.10-100.00 mm.s^{-1}. We adjust film thickness (h) to be comparable across the substrates by slightly varying solution concentration (C) at a specific v (Figure 3a). This implies that the evaporation rate (Q_{evap}) in the evaporation regime should be different on various templates given the mass balance equation[48]: $Q_{evap} = \frac{C}{hL\rho} v^{-1}$, where solution density (ρ) and film width (L) are fixed. Figure 3b-c summarizes our Q_{evap} calculations using this relationship. The fastest Q_{evap} values are obtained when coating on IL templates, which are 25% and 50% higher compared to coating on EG and GLY, respectively. These results are qualitatively consistent with solution-substrate enthalpy of interactions measured via ITC (Figure S1c). This is because stronger solution-template interaction is correlated with higher work of adhesion which decreases the solution-template interfacial free

energy ($\gamma_{solution\text{-}template}$)[49]. Based on Young's equation[50], lower $\gamma_{solution\text{-}template}$ corresponds to smaller contact angle which leads to higher evaporation rate.

We postulate that stronger template-CP interactions increase polymer concentration at substrate-solution interface during MGC, shown by MD simulations in our previous work[30]. This phenomenon potentially decreases the free energy barrier to heterogenous nucleation and expedites CP surface-induced nucleation. Thus, CP crystallization would be enhanced and depending on the coating regime flow-induced unidirectional alignment can be improved. We test this hypothesis by characterizing solution-coated DPP-BTz thin film multiscale morphology via AFM, C-POM, UV-vis spectroscopy and GIXD. Primarily, we focus on the influence of template properties on the thinnest films coated at 1.00 mm.s^{-1}. The effect of coating speed will be discussed at the end.

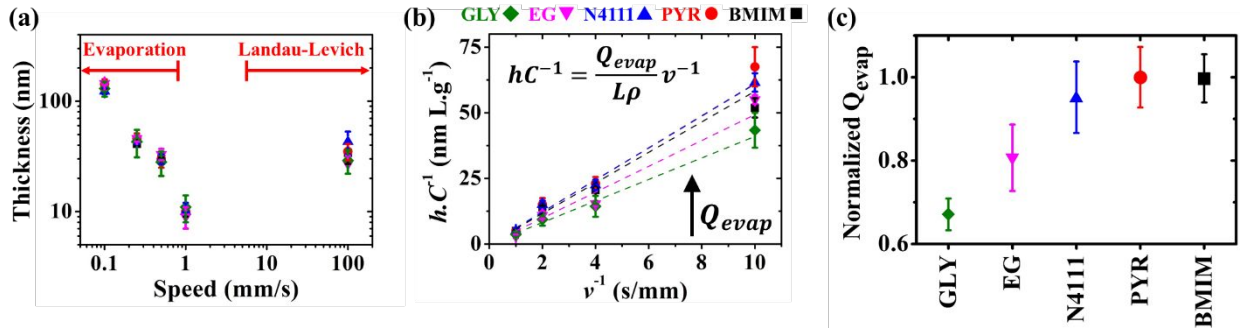

Figure 3. Quantifying evaporation rate from coating speed-dependent thickness measurements. a) DPP-BTz film thickness, h, as a function of deposition speed ranging from 10-140 nm measured by AFM. Evaporation and Landau-Levich regimes can be characterized at low and high coating speeds, respectively. (b) h.C^{-1} vs. v^{-1} plot with the corresponding linear fit dashed lines. The slope in this plot is proportional to evaporation rate. (c) Corresponding normalized Q_{evap} across various templates. These results reveal higher evaporation rate on templates with stronger interaction with the DPP-BTz solution.

After fabricating DPP-BTz films via MGC on different templates they are transferred to octadecyltrichlorosilane (ODTS)-modified silicon substrates to enable direct morphology and

device comparison. We prob mesoscale topology of DPP-BTz thin films in direct contact with the template by AFM. Figure 4 shows AFM height images exhibiting semi-crystalline domains perpendicular to the coating direction. Domain size increases as the template-CP interaction becomes stronger. Film thickness is fixed at 10±1 nm which is estimated to be 3-4 molecular layers. GLY-coated films have significantly smaller domains compared to films coated on EG and ILs due to its slower template dynamics. BMIM- and PYR-templated films have the largest domains exceeding several microns in width corresponding to their strong interaction with DPP-BTz. Such drastic difference in morphology persisted across the entire coating speed (film thickness) series as discussed later.

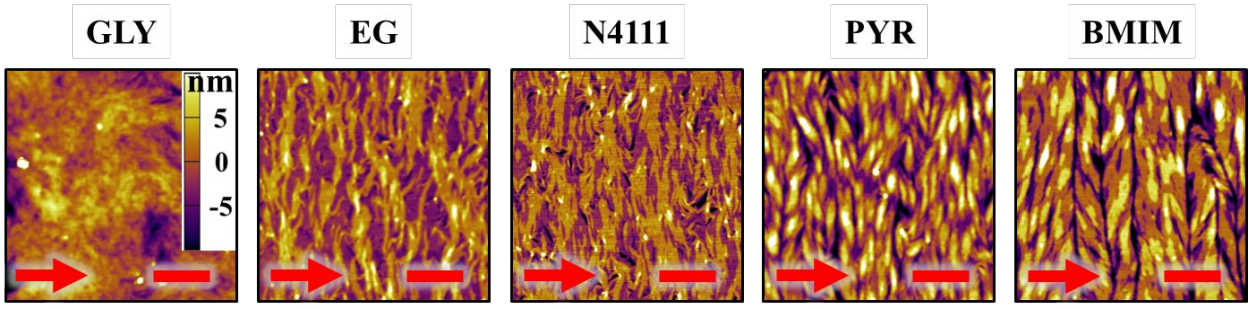

Figure 4. Atomic force microscopy for obtaining DPP-BTz film meso-scale morphology and thickness. Tapping mode AFM height images of DPP-BTz films obtained by MGC at 1.0 mm.s^{-1} on various dynamic templates. All scale bars are 1 μm. Crystalline domain size is the largest on BMIM and the minimum on GLY.

Next, we investigate macroscale morphology and polymer backbone orientation using C-POM (Figure 5a) and UV-vis spectroscopy (Figure 5b) demonstrating highly aligned films obtained from more dynamic templates. Regarding C-POM, an uniaxially aligned film exhibits the maximum (minimum) brightness when the polymer backbone is oriented 45° (0° or 90°) with respect to the cross-polarizer axis. The difference in brightness comparing images oriented 0° and

45° relative to the coating direction is defined as the optical birefringence which is a measure of the extent of alignment. Figure 5a shows that GLY-coated DPP-BTz films are almost isotropic while films deposited on EG and IL dynamic templates are uniaxially aligned. We quantify the extent of polymer chain alignment from C-POM birefringence and UV-vis dichroic ratio. To quantify the C-POM images birefringence, we use "Image J" image analysis software[51]. We extract the mean intensity values for images taken parallel (I_0) and 45 degrees rotated (I_{45}) with respect to the coating direction and calculate the anisotropy using intensity difference= $\frac{I^{45} - I^{0}}{I^{0}}$. Although image brightness and the value of I are a function of thickness, intensity difference is independent of film thickness by definition. Figure 5c compares C-POM birefringence for different substrates. Intensity difference for isotropic GLY-templated films is close to 1 and exceeds 2 for EG- and ILs-coated films given their anisotropy.

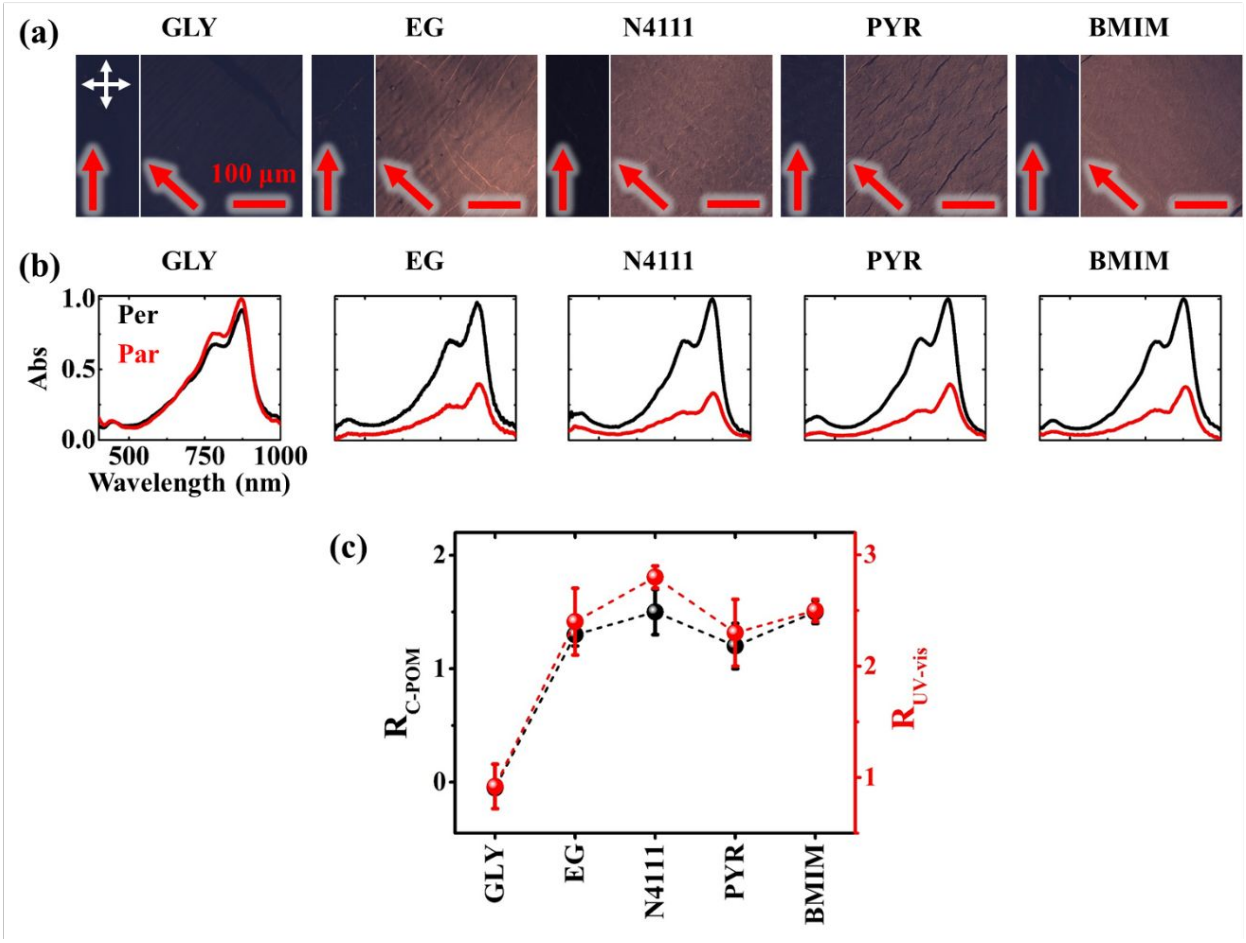

Figure 5. Macroscale morphology and alignment of DPP-BTz films. (a) Cross-polarized optical microscopy images of DPP-BTz films coated at 1.0 mm.s^{-1}. Crossed polarizers orientation is shown as white crossed arrows and the red single arrows show the coating direction (all scale bars are 100 µm). Upon rotating samples, the whole C-POM image illuminates indicating a uniform uniaxial macroscale alignment. (b) Normalized absorption spectra of polarized ultraviolet–visible spectroscopy comparing DPP-BTz films oriented parallel (red) and perpendicular (black) to the coating direction. (c) C-POM intensity difference (black) and $R_{UV\text{-}vis}$ (red) values calculated for DPP-BTz films coated on template series. C-POM intensity difference is calculated from the following equation: $\frac{I^{45} - I^{0}}{I^{0}}$ where I_{45} and I_0 are the average intensities when the film is oriented 45^0 vs. 0^0 with respect to the polarizer axis shown in Figure 5a. $R_{UV\text{-}vis}$ is calculated

from the ratio of 0-0 vibrational peak intensity perpendicular (I_{per}) and parallel (I_{par}) to the coating direction, $R_{UV\text{-}vis}=\frac{I_{per}}{I_{par}}$.

To further evaluate preferential orientation of the polymer backbone and the extent of macroscale alignment, we perform polarized UV-vis spectroscopy measurements. Upon applying linearly polarized light, the maximum (minimum) absorbance is observed as the transition dipole moment (TDM) align with (is transverse to) the polarizer vector. For CPs TDM have the largest component along the backbone[52-54]. Polarized UV-Vis measurements reveal that the polymer backbone is preferentially oriented perpendicular to the coating direction for films coated on ILs and EG, but the GLY-templated films are isotropic. We further quantify the degree of alignment using the 0-0 vibrionic peak dichroic ratio ($R_{UV\text{-}vis}$) (Figure 5c). $R_{UV\text{-}vis}$ is defined as the ratio between 0-0 peak absorbance perpendicular and parallel to the polarizer. $R_{UV\text{-}vis}$ for GLY is ~1 as expected but exceeded 2.5 for the EG and IL templates due to better alignment, consistent with C-POM results. It should be noted that $R_{UV\text{-}vis}$ provides a lower bound to the degree of backbone alignment since TDM is not necessarily aligned with the backbone depending on its curvature[52, 55]. Moreover, the highest $R_{UV\text{-}vis}$ (> 8) is obtained at lower coating speeds (0.1-0.25 $mm.s^{-1}$) which will be discussed later.

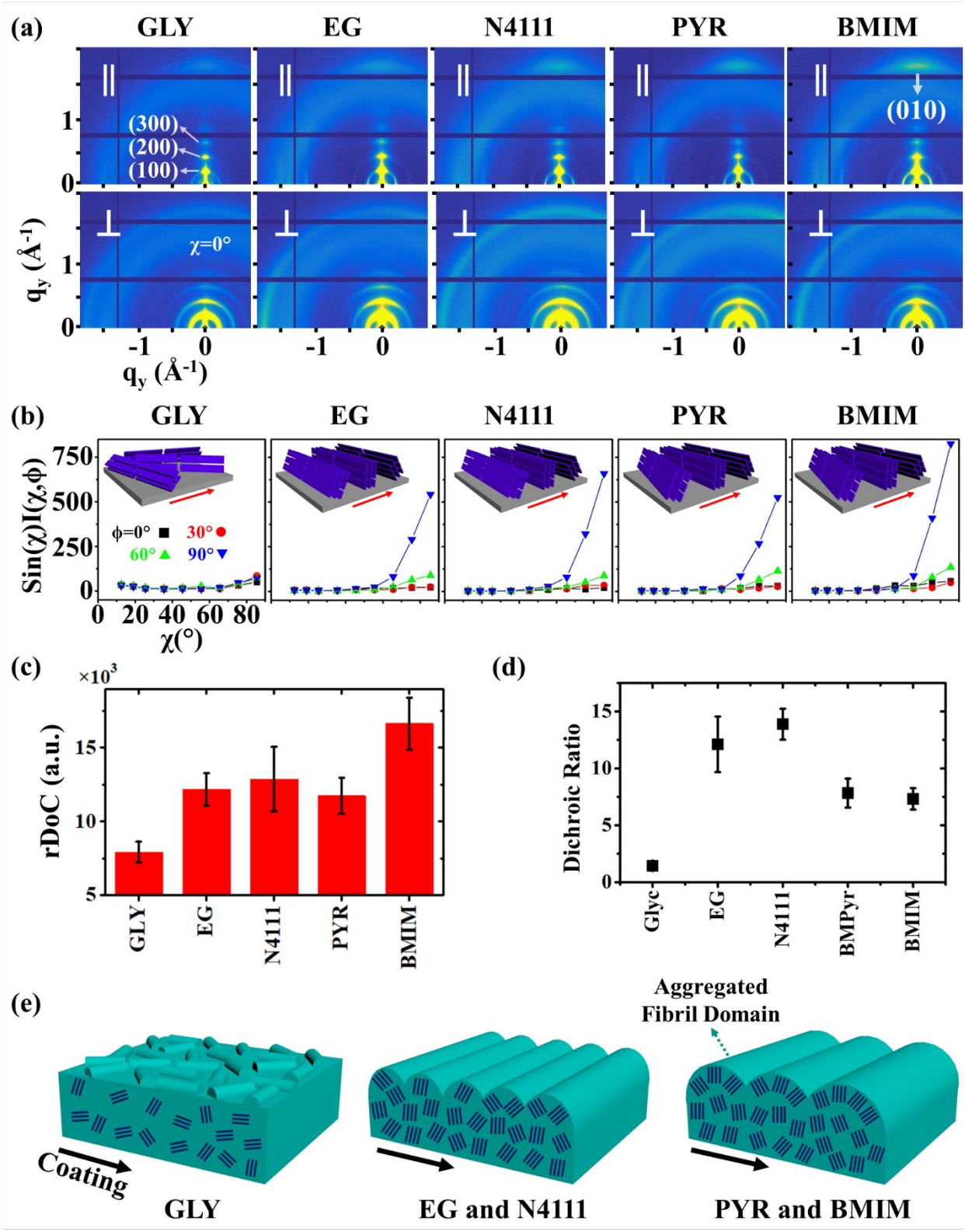
(a)
GLY
EG
N4111
PYR
BMIM
(300)
(200)
(100)
(010)
χ=0°
q_y (Å^{-1})
q_y (Å^{-1})
(b)
GLY
EG
N4111
PYR
BMIM
Sin(χ)I(χ,ϕ)
ϕ=0°
30°
60°
90°
χ(°)
(c)
×10^3
rDoC (a.u.)
GLY
EG
N4111
PYR
BMIM
(d)
Dichroic Ratio
Glyc
EG
N4111
BMPyr
BMIM
(e)
Aggregated
Fibril Domain
Coating
GLY
EG and N4111
PYR and BMIM

Figure 6. GIXD analysis of DPP-BTz thin films coated on various substrates. (a) GIXD micrographs of DPP-BTz thin films coated on various templates with the incident beam oriented parallel (||) (φ= 0°) and perpendicular (⊥) (φ= 90°) to the coating direction. DPP-BTz films are transferred to ODTS-treated SiO_2 prior to the measurement. (100) peak intensity and azimuthal spread in parallel and perpendicular scans are not similar due to the deviations from idea edge-on stacking. (b) Geometrically corrected intensity of DPP-BTz π−π stacking (010) peak as a function of pole angle χ and substrate in-plane rotation angle φ. Measurements are performed at different in-plane rotation angles of the substrate: φ= 0°, 30°, 60° and 90° with respect to the incident beam. Path length corrected intensity is obtained from a sector cut on GIXD image with -88°<χ<-83° at φ= 0°, 30°, 60° and 90°. Peak intensities are normalized by the irradiated volume to allow direct comparison among various films. Dominant crystallite orientation is shown in the insets. 'Face-on' crystallites are described by the (010) peak at χ=90° and the (100) peak at χ=0°, and the 'edge-on' crystallites by the (010) peak at χ=0° and the (200) peak at χ=90°. (c) Relative degree of crystallinity (rDoC) for various templates calculated from: $rDoC \propto \int_0^{\frac{\pi}{2}}\int_0^{\frac{\pi}{2}} \sin(\chi) I(\chi, \varphi) d\chi d\varphi$. Standard errors are calculated from (010) peak area multipeak fittings. (d) GIXD dichroic ratio (R_{GIXD}) calculated from $R_{GIXD} = \frac{A_{per}}{A_{par}}$, where A_{per} (A_{par}) is edge-on π-π stacking peak perpendicular (parallel) to the coating direction. (e) Illustration of morphology model inferred from GIXD and AFM shown in Figure 4.

We next employ GIXD to resolve DPP-BTz thin film molecular packing and quantify relative degree of crystallinity (rDoC). Analyzing π-π stacking peaks further reveal higher crystallinity of DPP-BTz films coated on templates with stronger interaction with the CP. Figure 6a shows GIXD micrographs scanned parallel and perpendicular to the coating direction. GLY-coated films exhibit weak isotropic π-π stacking. However, films coated on EG and ILs exhibit well-defined edge-on π-π stacking peaks (010). To quantitatively analyze the orientation distribution of π-crystallites, we extract pole figures[56] following procedures described in our previous report[23]. Figure 6b shows

π-π stacking peak (010) intensities as a function of the polar angle χ and the in-plane rotation angle of the substrate, φ. We infer from these figures that GLY-coated films adopt a bimodal distribution of edge-on and face-on crystallites with weak π-π diffractions. However, films coated on EG and ILs exhibit sharp peaks characteristic of 'edge-on' orientation. We further calculate the relative degree of crystallinity (rDoC) of DPP-BTz thin films by integrating the geometrically corrected peak intensities over χ and φ (Figure 6c). Increasing the strength of template-DPP-BTz interaction lead to higher relative degree of crystallinity. For films deposited on EG rDoC is >53% higher than GLY-templated films. BMIM-coated films have the highest rDoC value, >30% higher compared to those of EG, N4111 and PYR. This observation is consistent with the largest domain size for BMIM-coated films probed by AFM (Figure 4).

Regarding the polymer in-plane alignment, except isotropic GLY-coated films, we observe strong edge-on π-π stacking peaks in the perpendicular scans. Thus, the polymer backbone is preferentially oriented orthogonal to the coating direction as inferred from UV-vis data. We quantify this anisotropy via GIXD dichroic ratio (R_{GIXD}) described as the ratio between normalized edge-on π-π stacking peak perpendicular and parallel to the coating direction. Figure 6d plots R_{GIXD} values comparing all templates. For films deposited on EG, R_{GIXD} is >8.3 times higher than GLY representing a dramatic enhancement in polymer film alignment due to increased template dynamics of EG vs. GLY. We observe the highest R_{GIXD} for N4111 (R_{GIXD}=13.9±1.4) and not BMIM. We ascribe this to increased population of edge-on π-crystallites for BMIM-templated films in all directions even parallel to the coating direction (obvious from φ=0° $\sin(\chi)I(\chi,\varphi)$) due to its higher rDoC. Figure 6e summarize the suggested molecular packing within aggregated fibrillar domains across the template series.

Coating speed-dependent multiscale morphology. To evaluate the generality of our observations, we further investigate the influence of coating speed on template-directed multiscale morphology of DPP-BTz thin films. Coating speed (v) is modulated from 0.10 to 100.00 mm.s^{-1} covering both the evaporation regime and the Landau-Levich regime[48] (Figure 3a). After transferring the polymer films from liquid templates to ODTS substrates, the mesoscale morphology of DPP-BTz film directly in contact with templates is characterized by AFM (Figures S2 and 7a). The largest domains are observed on BMIM-templated films, whereas the GLY-coated films don't exhibit clearly defined fibril structures and domains. While this trend is clearer in the evaporation regime (<1 mm.s^{-1}), it persists across the entire range of coating speeds studied (Figure 7a). Interestingly, even in the Landau-Levich regime (100.00 mm.s^{-1}), the mesoscale morphology is sensitive to the choice of template, indicating that the template-induced crystallization outcompetes that from the ink-air free surface. At this condition, the crystallite size of IL-templated films is as large as 10 µm, compared to 1-2 µm for EG-templated films and sub-micron domains on GLY. This observation is further confirmed via high magnification C-POM images (Figure 7b). In addition, C-POM images brightness (intensity) increase in the following order: GLY<EG<PYR~N4111<BMIM. Higher C-POM image brightness is ascribed to higher relative crystallinity of IL-templated films which is further verified by GIXD measurements.

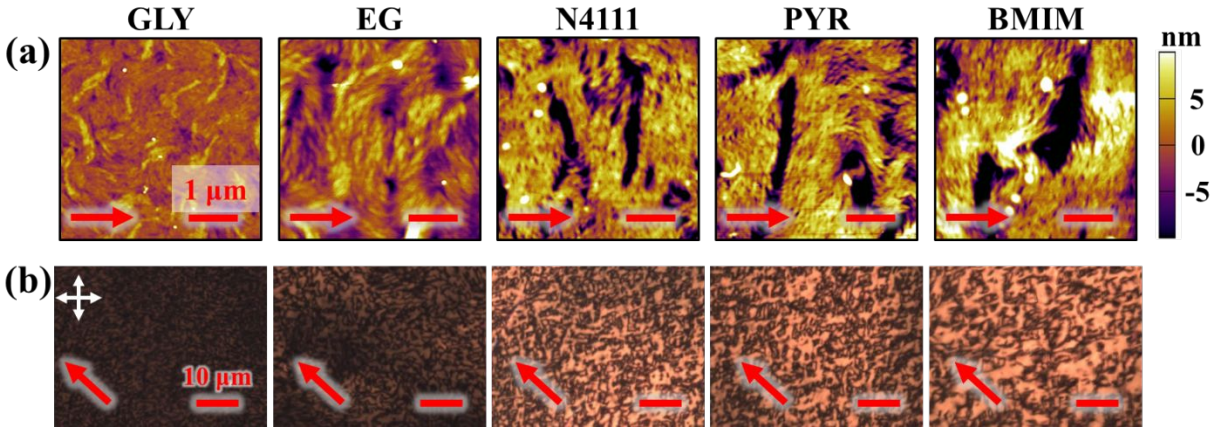

Figure 7. Meso-scale morphology of DPP-BTz films obtained in Landau-Levich regime. (a) Tapping-mode AFM height images (1 μm scale bars) and (b) high magnification C-POM images of DPP-BTz film coated on various templates at 100 mm.s^{-1}. The arrow indicates the coating direction. Even at this high coating speed the meso-scale morphology of CP film is sensitive to template properties.

Speed-dependent C-POM (Figure S3) and UV-vis (Figure S4) results reveal printing-regime-dependent in-plane alignment. At low speeds (0.10-0.50 mm.s^{-1}) solvent evaporation at the three-phase contact line induces nucleation. Thus, film growth follows the receding meniscus resulting in aligned domains (evaporation regime). C-POM intensity difference ($R_{UV\text{-}vis}$) for EG films is 7-22 (3-4) times higher than GLY films in this regime (Figure 8). In-plane alignment is comparable for EG and ILs with maximum C-POM intensity difference and $R_{UV\text{-}vis}$ exceeding 33 and 8 for films printed at 0.1 mm.s^{-1} on N4111. However, in the Landau-Levich regime (100 mm.s^{-1}) viscous force becomes predominant and produces isotropic domains.

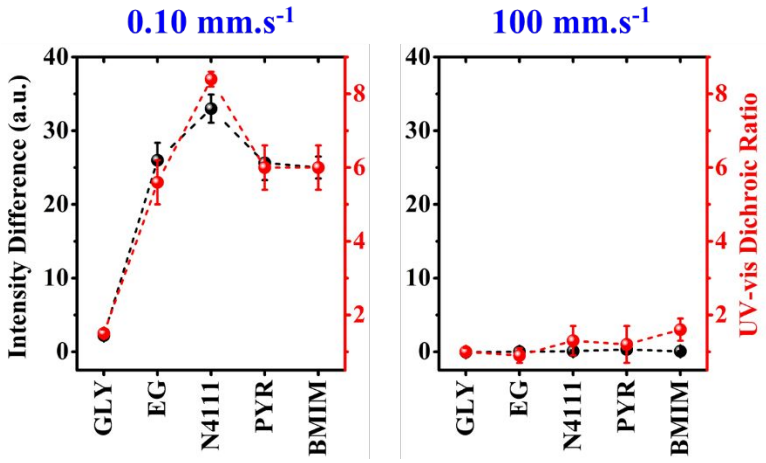

Figure 8. Comparing macroscale alignment of DPP-BTz films coated in the evaporation vs. Landau-Levich regimes. Intensity difference from C-POM (black) and $R_{UV\text{-}vis}$ (red) values calculated for DPP-BTz films coated on template series at 0.10 and 100 mm.s^{-1}.

We then employ GIXD to characterize out-of-plane molecular orientation distribution and determine the relative degree of crystallinity in the evaporation (v=0.1 mm.s^{-1}) and Landau-Levich regime (v=100.00 mm.s^{-1}) (Figure 9 and Figure S5-6). Pole figure analysis shows preferential edge-on packing for all cases. Films coated at 0.1 mm.s^{-1} exhibit a broader out-of-plane orientation distribution than thinner films coated at 1.00 mm.s^{-1} which may arise from increasing importance of bulk nucleation as opposed to template-induced nucleation for thicker films. The in-plane alignment of π-crystallites (Figure S5b) is consistent with the trend observed from C-POM and UV-vis at 0.1 mm.s^{-1}. Specifically, the average GIXD dichroic ratio (R_{GIXD}) increases from 1.4±0.2 to 12.1±2.4 comparing GLY with EG, and the maximum value is observed for N4111 being 13.9±1.4. In addition, we observed that the full width at half maximum (FWHM) of the π-π stacking peak is almost 48% larger on GLY compared to the other templates at 0.1 mm.s^{-1} (Figure S5c). This can be attributed to lower crystalline order and/or smaller domain size in GLY-templated films due to slow template dynamics. π-π stacking distance only slightly varies across the templates (3.62±0.02 Å) (Figure S5d).

We next estimate rDoC for films coated at 0.1 and 100.00 mm.s^{-1} from their corresponding pole figures (Figure 9a-d). Once again, our analysis confirmed that CP films exhibit higher crystallinity on templates with stronger interactions with DPP-BTz. Films coated on BMIM are >200% more crystalline compared to EG, PYR and N4111 at 0.1 and >30% at 100 mm.s^{-1}. Overall, our characterizations demonstrate that across a wide range of coating speed (and film thickness) template dynamics and chemistry can influence multiscale morphology significantly. This dependence is consistently correlated with the strength of template-CP interaction (Figure 2b).

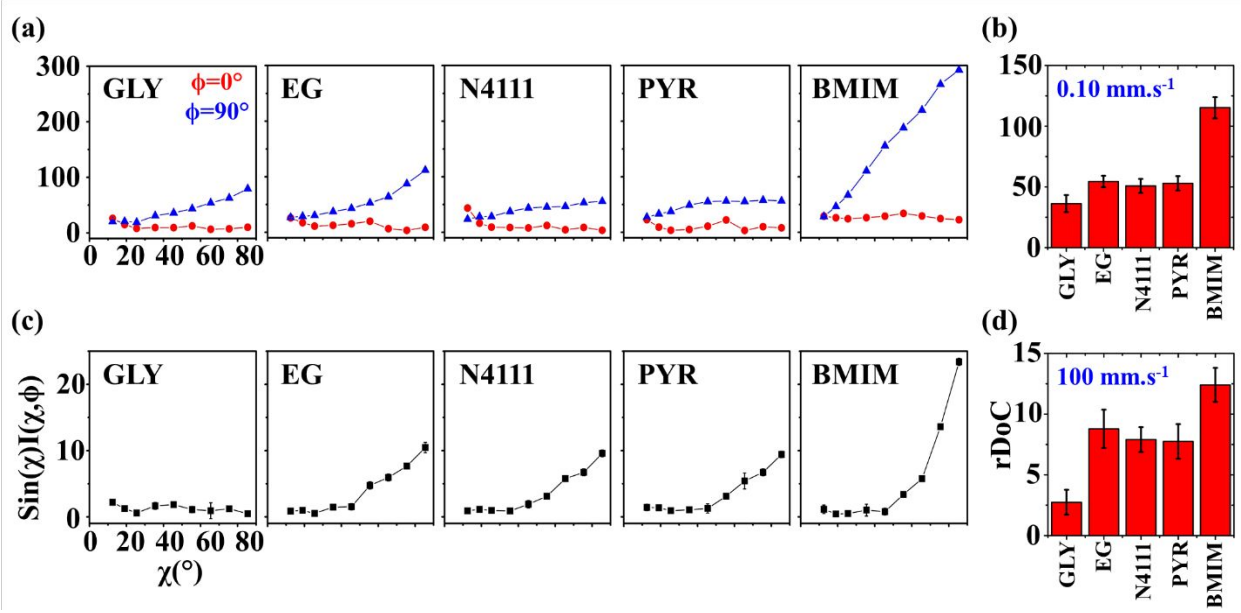

Figure 9. GIXD analysis of templated DPP-BTz thin films comparing evaporation and Landau-Levich regimes. Geometrically corrected intensity of DPP-BTz π–π stacking (010) peak ($I(\chi, \varphi)$ and corresponding estimated rDoC for the series of templates coated at (a, b) 0.10 and (c, d) 100.00 mm.s^{-1}. Measurements are performed at φ= 0° and 90° for films coated at 0.10 mm.s^{-1} and the rDoC is roughly estimated from: $rDoC \propto \int_0^{\frac{\pi}{2}}\int_0^{\frac{\pi}{2}} \sin(\chi) I(\chi, \varphi) d\chi d\varphi$. However, because the film coated at 100.00 mm.s^{-1} is isotropic (based on C-POM and UV-vis) we estimate the rDoC value only from the ϕ= 0° measurement from: $rDoC \propto \int_0^{\frac{\pi}{2}} \sin(\chi) I(\chi) d\chi$. Standard errors are calculated from (010) peak area multipeak fittings. Corresponding GIXD micrographs are represented in Figures S5a and S6.

Morphology-Dependent Field-Effect Transistor Performance. Finally, we establish morphology-charge transport relationship in DPP-BTz films by fabricating FET devices parallel and perpendicular to the coating direction (Figure 10a-c). Device configuration is depicted in Figure 10a and fabrication details are described in the Experimental section. Representative transfer, output and gate voltage (V_G)-dependent plots are summarized in Figure S7-S9. FETs fabricated from DPP-BTz films templated on ILs exhibit the highest average apparent hole

mobility (μ_{app}) due to their stronger interactions with CP (Figure 10c). For polymer films coated in the evaporation regime, μ_{app} is predominantly larger perpendicular to the coating direction. This excludes GLY-coated films at 0.25-1.00 mm.s^{-1} given the lack of anisotropy and low crystallinity. More efficient charge transport perpendicular to the coating direction is mainly explained by faster charge transport along polymer backbone facilitated by enhanced in-plane molecular alignment, larger domains (less grain boundaries) and higher rDoC. The highest performing device is obtained from BMIM-templated films coated at 1.00 mm.s^{-1} with active channel orthogonal to the coating direction. Transfer and output characteristics for the corresponding p-channel device is shown in Figure 10b with μ_{app} exceeding 2.8 cm^{2}V^{-1}s^{-1}. This is >5 times higher than μ_{app} parallel to the coating direction. Such charge transport anisotropy is not surprising given the high in-plane alignment of the polymer backbone. Films coated in the Landau-Levich regime (100 mm.s^{-1}) show μ_{app} less than 1.0 cm^{2}V^{-1}s^{-1} with no charge transport anisotropy. At this condition, the μ_{app} values on IL-coated films are almost an order of magnitude higher than EG, and EG μ_{app} is >5 higher than GLY. These results agree with the trend observed from crystallite size analysis and rDoC for the 100 mm.s^{-1} coating speed.

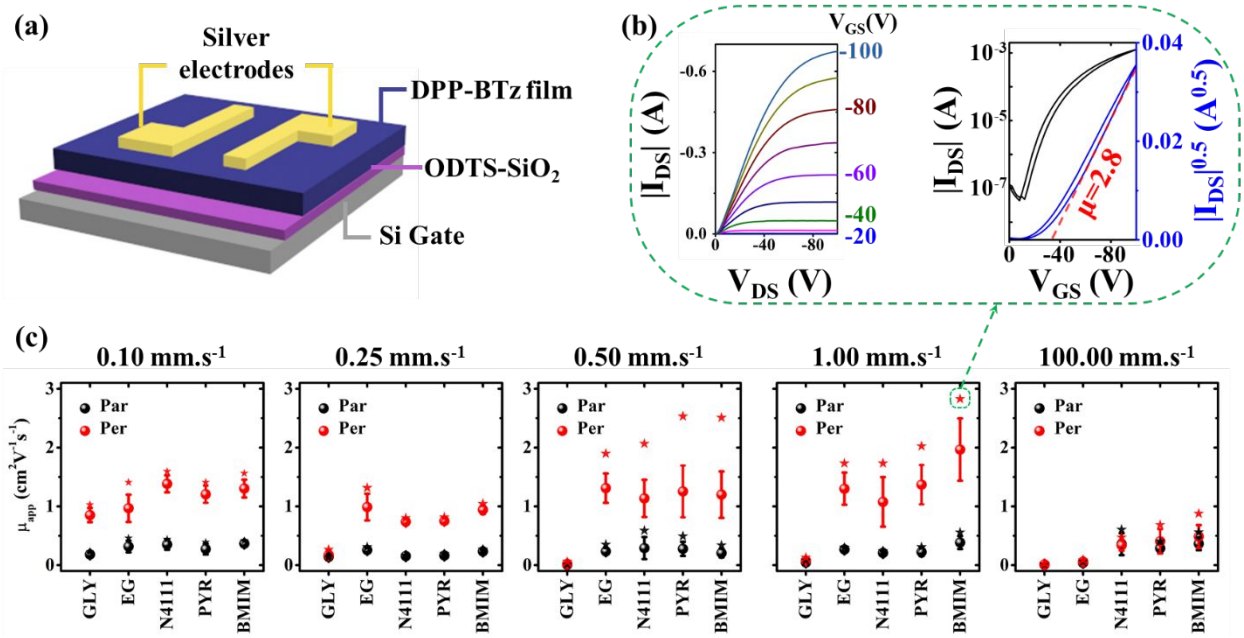

Figure 10. (a) Bottom-gate top-contact OFET device. (b) Highest performing device obtained from DPP-BTz film printed at 1 mm.s^{-1} on [BMIM][TFSI] dynamic template. On/off ratio and threshold voltage are 2.9×10^4 and -18.8 V, respectively. (c) Comparing apparent mobility of DPP-BTz OFET devices with active channel perpendicular and parallel to the coating direction across a wide range of speeds on various templates.

CONCLUSION

In conclusion, we establish that template-conjugated polymer interactions quantified by the enthalpy of adsorption. Interactions strength can serve as a unifying metric to gauge the effectiveness of dynamic templates in directing crystallization and assembly of conjugated polymers. Such template-conjugated polymer interactions are sensitive to both template dynamics and chemistry. To investigate the role of surface reconfigurability, we choose glycerol and ethylene glycol hydrogen-bonded liquids due to their similar chemistry and drastically different dynamics. Directly measuring template-conjugated polymer interactions using isothermal titration calorimetry (ITC) verifies that faster dynamics of ethylene glycol result in ~2 times stronger

interaction with the polymer compared to glycerol. Such difference in the strength of interactions directly impact solution-coated thin film morphology. Comparing DPP-BTz films coated on ethylene glycol vs. glycerol, AFM showed >10 times increase in semi-crystalline domain size, and C-POM and UV-vis demonstrated improved macroscopic alignment by up to 22- and 4-times. Moreover, GIXD demonstrates up to 3-fold higher relative degree of crystallinity and long-range order of semi-crystalline domains formed on ethylene glycol. Combination of these morphological changes results in up to an order of magnitude improvement in FET charge transport mobility. These results persist in the whole coating speed range from 0.1-100.00 $mm.s^{-1}$.

To further elucidate the role of template chemistry, we select 3 ILs with different cations and comparable dynamics with ethylene glycol. ILs $\Delta H_{interaction}$ measured by ITC is higher than ethylene glycol (N4111<PYR<BMIM). Consequently, semi-crystalline domain size observed from AFM and relative degree of crystallinity measured by GIXD are increasing with stronger template-polymer interactions. This trend is preserved in field-effect transistor device performance and IL-templated films exhibit highest charge transport mobility with the best-performing devices templated on BMIM. The observed trend is independent of coating speed and printing regimes, indicating that dynamic template plays a critical role in polymer crystallization regardless of coating conditions.

Based on these results we propose favorable interactions between conjugated polymer and template as a design rule for dynamic template-directed assembly. To enhance template-conjugated polymer interactions, not only should the template have functional groups to interact strongly with the conjugated polymer, but also its dynamics should be fast enough within the coating time-frame to interact effectively with the assembling polymer through surface reconfiguration. Compound effect of these two criteria leads to strong affinity of conjugated

polymer with the template as to enrich polymer molecules near the template interface. This phenomenon decreases the free energy barrier to nucleation, expedites nucleation and ensuing crystallization process. Our results establish the significant importance of substrate interfacial properties to semiconducting polymer crystallization during solution coating and printing as this important class of functional materials ripens for commercialization.

EXPERIMENTAL METHODS

Isothermal Titration Calorimetry measurements. ITC experiments were carried out using a Nano ITC Low Volume isothermal titration calorimeter (TA Instruments) at 298 K and data were extracted from NanoAnalyze software. Data was analyzed using Origin software. The accuracy of the instrument was verified by measuring water-water titration enthalpy before each series of measurements. Reaction cell was rigorously cleaned in two steps: 1-Cleaning the cell with series of NaOH, Formic acid and DI water, and 2-Rinsing the cell by isopropanol, chloroform and acetone. The cell was heated to 60°C to evaporate all residual solvents. Next, 50 µL of the liquid template was injected to the reaction cell and reference cell. We waited for 15 minutes to make sure the liquids descend completely to the bottom (30 minutes for higher viscosity glycerol), no residual liquid is stuck to the cells wall and avoid bubbles. Then 50 µL of 2 $g.L^{-1}$ DPP-BTz solution in chloroform was loaded to the injection syringe and mounted on the ITC instrument. We set the temperature to 298 K and the instrument thermal power was monitored until baseline returned to the initial value. We started all titration experiments with a 0.25 µL to avoid bubbles in the main experiment. After 30 minutes, 3 µL of the DPP-BTz solution was titrated on the liquid template. We then recorded heat flow as a function of time ($\mu J.s^{-1}$) for 60 minutes and repeated the experiment at least 3 times for each template. The average area under the curves was used to

calculate the adsorption heat of DPP-BTz to the template after subtracting the similar single-injection of pure solvent.

Substrate preparation. Semi-solid dynamic templates served as substrates compatible with large-scale solution coating. Dynamic templates were constructed by infiltrating nanoporous anodized aluminum oxide (AAO) Whatman® Anodisc membranes (purchased from Sigma-Aldrich) with various liquid templates supported by glass substrates. AAO had 200 nm pore size and its diameter was 1.3 mm. Hydrogen-bonded liquids include glycerol (GLY) (99.6% ACS-grade purchased from Fisher Scientific) and ethylene glycol (EG) (99.8% anhydrous purchased from Sigma-Aldrich). Bistriflimide-based ionic liquids (99%) were purchased from IoLiTec Ionic Liquids Technologies Inc. and stored in nitrogen glove box prior to use as received. ILs include 1-butyl-3-methylimidazolium bis(trifluoromethylsulfonyl)imide ([BMIM][TFSI]), 1-butyl-1-methylpyrrolidinium bis(trifluoromethylsulfonyl)imide ([PYR][TFSI]) and 1-butylammonium-1,1,1-trimethylammonium bis(trifluoromethylsulfonyl)imide ([N4111][TFSI]).

Meniscus-guided coating for conjugated polymer thin film fabrication. The semiconducting polymer, Poly[[2,5-bis(2-octadecyl)-2,3,5,6-tetrahydro-3,6-diketopyrrolo[3,4-c]pyrrole-1,4-diyl]-alt-(2-octylnonyl)-2,1,3-benzotriazole] (DPP-BTz) (M_n=176 kg.mol^{-1} and PDI=2.5) was synthesized as previously reported[32] and used as received. We prepared DPP-BTz solution by dissolving the polymer in anhydrous chloroform (Macron ACS grade) on a stirring hot plate at 50°C until obtaining a clear homogeneous solution (> 2 hours). DPP-BTz thin films were deposited onto templates by meniscus-guided coating (MGC)[23, 30]. The MGC setup included a stationary substrate and a moving dewetting coating blade, with polymer solution sandwiched in between. The blade was tilted 8° and blade-substrate gap was fixed at 100 μm. All films are deposited at substrate temperature of 25 °C with varying coating speed of 0.10-100 mm.s^{-1}. Solution

concentration was modulated between 2.0-3.0 $g.L^{-1}$ to obtain comparable film thickness across all substrates. After coating DPP-BTz films on liquid/AAO hybrid substrates, they were transferred to octadecyltrichlorosilane (ODTS) functionalized silicon wafer with 300nm thermally grown SiO2 by simply bringing the substrate in contact with the film. ODTS-modified substrate served as mutual substrate for morphology characterizations and device fabrication enabling direct comparison across substrates (see previous reports[23, 30] for ODTS modification details). After removing the AAO membrane, the transferred films were subsequently immersed in acetonitrile for at least 5 minutes to remove the residual liquids.

DPP-BTz thin film multiscale morphology characterizations. We used a Nikon Ci-POL optical microscope to visualize the as-fabricated polymer thin film microstructure and assess uniaxial alignment under cross-polarized light. Birefringence was quantified using Image J analysis software[51]. Meso-scale morphology of the film in direct contact with template during MGC was characterized using tapping mode Asylum Research Cypher atomic force microscope. Film thickness was measured using AFM height image cross-sections. Polarized UV−Vis absorption spectra were collected at room temperature on an Agilent Cary 60 UV-Vis spectrophotometer, with and without the incident light polarized vertically by a broadband sheet polarizer. Measurement data was obtained using the as-coated films on the template/AAO/glass structure after subtracting the background within the wavelength of 400-1000 nm. Grazing-incidence X-ray diffraction (GIXD) was performed at the small-wide-angle X-ray scattering beamline 8-ID-E at the Advanced Photon Source (Argonne National Laboratory) with an X-ray wavelength of 1.6871 Å (E_{beam}=7.35 keV), at a 208 mm sample-to-detector distance[57]. A two-dimensional Pilatus 1M detector was used for data collection. The incidence angle was 0.14° and the exposure time was 10-30 s. During the measurement, the samples were placed in a helium

chamber, with a 228-mm sample-to-detector distance. Each sample was scanned at various in-plane rotation angles (φ) by rotating the substrate with respect to the incidence beam by 0°, 30°, 60° and 90°. Herein, φ is defined as 0° when the film coating direction is oriented parallel to the incident beam. Data analysis was performed with the software GIXSGUI, which included a correction for the polarization of the synchrotron x-ray beam[56, 58]. The edge-on π-π stacking peak and the lamella stacking peak were obtained from a sector cut between $-88^0<\chi<-83^0$ and $-10^0<\chi<-5^0$ respectively from the geometrically corrected image. Partial pole figures were constructed by extracting (010) π-π stacking peak intensities as a function of the polar angle χ (13-88° binned into ~5° increments) to analyze domain orientation distribution, as well as relative degree of crystallinity. To accurately calculate the peak intensities, multipeak fitting was performed with Igor Pro on the intensity vs. q curve obtained from each 5° segment along the χ axis. The purpose was to deconvolute the π-π stacking peak from the amorphous ring, SiO_2 scattering and the ODTS peak. The peak intensity and area thus obtained were further normalized by the film thickness and beam irradiated area on the films. The background diffractions of all substrates were also carried out under the same condition. The π-π stacking peak was fitted with a Lorentzian function to obtain the peak position and peak area for determining π-π stacking distance and dichroic ratio. The peak area was further normalized by the irradiated volume to allow comparison across samples.

Conjugated polymer FET fabrication and electrical characterization. We fabricated bottom-gate top-contact FETs by transferring the as-coated DPP-BTz semiconducting polymer film to a highly n-doped Si (gate) with thermally grown 300 nm SiO_2 modified by ODTS (dielectric layer) to minimize interfacial charge traps[59]. Silver source and drain electrodes of 45 nm thick were thermally evaporated onto the polymer films through a shadow mask. The channel length (L) was

47 μm and channel width (W) was 840 μm. All electrical measurements were performed in a nitrogen environment using a Keysight B1500A semiconductor parameter analyzer at room temperature. The field-effect mobilities in the saturation regime were calculated from $I_{DS} = \frac{WC_i\mu_{app}}{2L}(V_G - V_{th})^2$, where I_{DS} is the drain-source current, C_i is the dielectric capacitance per unit area (11 nF/cm^2 for ODTS-treated 300 nm SiO_2 dielectric), V_G is the gate voltage, μ is the apparent carrier mobility, and V_T is the threshold voltage. Average data were calculated from analysis of at least 10 independent devices.

Corresponding Author

*E-mail: yingdiao@illinois.edu

Conflicts of interest

There are no conflicts to declare.

Author Contributions

E. M. and Y. D. designed the research project and Y. D. supervised the project. E. M. carried out the experiments and analyzed all the corresponding data. G. Q. and P. K. performed the GIXD measurements and E. M. analyzed the data. Semiconducting polymer synthesis was done by J. K. L. and S. H. J. All authors discussed, revised, and approved the manuscript.

Acknowledgements

This work was funded primarily by the National Science Foundation, NSF DMR Award #18-47828. E.M acknowledges partial support by the NSF IMRSEC: Illinois Materials Research Center under grant number DMR 17-20633. Y.D. acknowledges partial support from the Jiangsu Industrial Technology Research Institute (JITRI) through the JITRI International Fellowship Program. This research used resources of the Advanced Photon Source, a U.S. Department of Energy (DOE) Office of Science User Facility operated

for the DOE Office of Science by Argonne National Laboratory under contract no. DE-AC02-06CH11357. We appreciate helps from beamline scientist Strazalka Joseph W. of Advanced Photon Source, Argonne National Laboratory facilitating the GIXD measurements. Part of this research was performed in the Frederick Seitz Materials Research Laboratory Central Facilities, University of Illinois.

REFERENCES

1. Tang, W.; Huang, Y.; Han, L.; Liu, R.; Su, Y.; Guo, X.; Yan, F., Recent progress in printable organic field effect transistors. *J. Mater. Chem. C* ***7***, 790-808 (2019).
2. Khim, D.; Luzio, A.; Bonacchini, G. E.; Pace, G.; Lee, M.-J.; Noh, Y.-Y.; Caironi, M., Uniaxial Alignment of Conjugated Polymer Films for High-Performance Organic Field-Effect Transistors. *Adv. Mater.* ***30***, 1705463 (2018).
3. Liu, Z.; Zeng, D.; Gao, X.; Li, P.; Zhang, Q.; Peng, X., Non-fullerene polymer acceptors based on perylene diimides in all-polymer solar cells. *Solar Energy Materials and Solar Cells* ***189***, 103-117 (2019).
4. Liu, Z.; Wu, Y.; Zhang, Q.; Gao, X., Non-fullerene small molecule acceptors based on perylene diimides. *Journal of Materials Chemistry A* ***4***, 17604-17622 (2016).
5. Moon, H. C.; Lodge, T. P.; Frisbie, C. D., Solution Processable, Electrochromic Ion Gels for Sub-1 V, Flexible Displays on Plastic. *Chem. Mater.* ***27***, 1420-1425 (2015).
6. McQuade, D. T.; Pullen, A. E.; Swager, T. M., Conjugated Polymer-Based Chemical Sensors. *Chem. Rev.* ***100***, 2537-2574 (2000).
7. Zhang, F.; Qu, G.; Mohammadi, E.; Mei, J.; Diao, Y., Solution-Processed Nanoporous Organic Semiconductor Thin Films: Toward Health and Environmental Monitoring of Volatile Markers. *Adv. Funct. Mater.* ***27***, (2017).
8. Himmelberger, S.; Salleo, A., Engineering semiconducting polymers for efficient charge transport. *MRS Commun.* ***5***, 383-395 (2015).
9. Venkateshvaran, D.; Nikolka, M.; Sadhanala, A.; Lemaur, V.; Zelazny, M.; Kepa, M.; Hurhangee, M.; Kronemeijer, A. J.; Pecunia, V.; Nasrallah, I.; Romanov, I.; Broch, K.; McCulloch, I.; Emin, D.; Olivier, Y.; Cornil, J.; Beljonne, D.; Sirringhaus, H., Approaching disorder-free transport in high-mobility conjugated polymers. *Nature* ***515***, 384 (2014).
10. Noriega, R.; Rivnay, J.; Vandewal, K.; Koch, F. P.; Stingelin, N.; Smith, P.; Toney, M. F.; Salleo, A., A General Relationship between Disorder, Aggregation and Charge Transport in Conjugated Polymers. *Nat. Mater.* ***12***, 1038 (2013).
11. Wittmann, J. C.; Lotz, B., Epitaxial crystallization of polymers on organic and polymeric substrates. *Prog. Polym. Sci.* ***15***, 909-948 (1990).
12. Binsbergen, F. L., Natural and artificial heterogeneous nucleation in polymer crystallization. *J. Polym. Sci. Polym. Symp.* ***59***, 11-29 (1977).
13. Bijal, B. P.; Ying, D., Multiscale assembly of solution-processed organic electronics: the critical roles of confinement, fluid flow, and interfaces. *Nanotechnology* ***29***, 044004 (2018).
14. Lee, W. H.; Cho, J. H.; Cho, K., Control of Mesoscale and Nanoscale Ordering of Organic Semiconductors at the Gate Dielectric/Semiconductor Interface for Organic Transistors. *J. Mater. Chem.* ***20***, 2549 (2010).
15. Joseph Kline, R.; McGehee, M. D.; Toney, M. F., Highly Oriented Crystals at the Buried Interface in Polythiophene Thin-Film Transistors. *Nat. Mater.* ***5***, 222 (2006).
16. Chabinyc, M. L.; Toney, M. F.; Kline, R. J.; McCulloch, I.; Heeney, M., X-ray Scattering Study of Thin Films of Poly(2,5-bis(3-alkylthiophen-2-yl)thieno[3,2-b]thiophene). *J. Am. Chem. Soc.* ***129***, 3226-3237 (2007).
17. Jimison, L. H.; Himmelberger, S.; Duong, D. T.; Rivnay, J.; Toney, M. F.; Salleo, A., Vertical confinement and interface effects on the microstructure and charge transport of P3HT thin films. *J. Polym. Sci. B Polym. Phys.* ***51***, 611-620 (2013).
18. Tseng, H.-R.; Ying, L.; Hsu, B. B. Y.; Perez, L. A.; Takacs, C. J.; Bazan, G. C.; Heeger, A. J., High Mobility Field Effect Transistors Based on Macroscopically Oriented Regioregular Copolymers. *Nano Lett.* ***12***, 6353-6357 (2012).

19. Chabinyc, M. L.; Lujan, R.; Endicott, F.; Toney, M. F.; McCulloch, I.; Heeney, M., Effects of the surface roughness of plastic-compatible inorganic dielectrics on polymeric thin film transistors. *Appl. Phys. Lett.* ***90***, 233508 (2007).
20. Jung, Y.; Kline, R. J.; Fischer, D. A.; Lin, E. K.; Heeney, M.; McCulloch, I.; DeLongchamp, D. M., The Effect of Interfacial Roughness on the Thin Film Morphology and Charge Transport of High-Performance Polythiophenes. *Adv. Funct. Mater.* ***18***, 742-750 (2008).
21. Kim, D. H.; Park, Y. D.; Jang, Y.; Yang, H.; Kim, Y. H.; Han, J. I.; Moon, D. G.; Park, S.; Chang, T.; Chang, C.; Joo, M.; Ryu, C. Y.; Cho, K., Enhancement of Field-Effect Mobility Due to Surface-Mediated Molecular Ordering in Regioregular Polythiophene Thin Film Transistors. *Adv. Funct. Mater.* ***15***, 77-82 (2005).
22. Kim, D. H.; Lee, H. S.; Shin, H.-J.; Bae, Y.-S.; Lee, K.-H.; Kim, S.-W.; Choi, D.; Choi, J.-Y., Graphene surface induced specific self-assembly of poly(3-hexylthiophene) for nanohybrid optoelectronics: from first-principles calculation to experimental characterizations. *Soft Matter* ***9***, 5355-5360 (2013).
23. Zhang, F.; Mohammadi, E.; Luo, X.; Strzalka, J.; Mei, J.; Diao, Y., Critical Role of Surface Energy in Guiding Crystallization of Solution-Coated Conjugated Polymer Thin Films. *Langmuir* ***34***, 1109-1122 (2018).
24. Guo, D.-Y.; Tsai, Y.-b.; Yu, T.-F.; Lee, W.-Y., Interfacial effects on solution-sheared thin-film transistors. *J. Mater. Chem. C* ***6***, 12006-12015 (2018).
25. Kim, C.; Facchetti, A.; Marks, T. J., Polymer Gate Dielectric Surface Viscoelasticity Modulates Pentacene Transistor Performance. *Science* ***318***, 76-80 (2007).
26. Noh, J.; Jeong, S.; Lee, J.-Y., Ultrafast formation of air-processable and high-quality polymer films on an aqueous substrate. *Nat. Commun.* ***7***, 12374 (2016).
27. Soeda, J.; Matsui, H.; Okamoto, T.; Osaka, I.; Takimiya, K.; Takeya, J., Highly Oriented Polymer Semiconductor Films Compressed at the Surface of Ionic Liquids for High-Performance Polymeric Organic Field-Effect Transistors. *Adv. Mater.* ***26***, 6430 (2014).
28. Pandey, M.; Pandey, S. S.; Nagamatsu, S.; Hayase, S.; Takashima, W., Solvent driven performance in thin floating-films of PBTTT for organic field effect transistor: Role of macroscopic orientation. *Org. Electron.* ***43***, 240-246 (2017).
29. Tripathi, A. S. M.; Pandey, M.; Sadakata, S.; Nagamatsu, S.; Takashima, W.; Hayase, S.; Pandey, S. S., Anisotropic charge transport in highly oriented films of semiconducting polymer prepared by ribbon-shaped floating film. *Appl. Phys. Lett.* ***112***, 123301 (2018).
30. Mohammadi, E.; Zhao, C.; Meng, Y.; Qu, G.; Zhang, F.; Zhao, X.; Mei, J.; Zuo, J.-M.; Shukla, D.; Diao, Y., Dynamic-template-directed multiscale assembly for large-area coating of highly-aligned conjugated polymer thin films. *Nat. Commun.* ***8***, 16070 (2017).
31. Schott, S.; Gann, E.; Thomsen, L.; Jung, S. H.; Lee, J. K.; McNeill, C. R.; Sirringhaus, H., Charge-Transport Anisotropy in a Uniaxially Aligned Diketopyrrolopyrrole-Based Copolymer. *Adv. Mater.* ***27***, 7356 (2015).
32. Gruber, M.; Jung, S.-H.; Schott, S.; Venkateshvaran, D.; Kronemeijer, A. J.; Andreasen, J. W.; McNeill, C. R.; Wong, W. W. H.; Shahid, M.; Heeney, M.; Lee, J.-K.; Sirringhaus, H., Enabling high-mobility, ambipolar charge-transport in a DPP-benzotriazole copolymer by side-chain engineering. *Chem. Sci.* ***6***, 6949-6960 (2015).
33. Qu, G.; Zhao, X.; Newbloom, G. M.; Zhang, F.; Mohammadi, E.; Strzalka, J. W.; Pozzo, L. D.; Mei, J.; Diao, Y., Understanding Interfacial Alignment in Solution Coated Conjugated Polymer Thin Films. *ACS Appl. Mater. Interfaces* ***9***, 27863-27874 (2017).
34. Böttcher, C. J. F.; Van Belle, O. C.; Bordewijk, P.; Rip, A., *Theory of Electric Polarization*. Elsevier, Amsterdam, Vol. II (1978).
35. Debye, P., *Polar Molecules*. Chemical Catalog Company, Inc., New York, NY, Vol. I (1929).

36. Segur, J. B.; Oberstar, H. E., Viscosity of Glycerol and Its Aqueous Solutions. *Ind. Eng. Chem. Res.* ***43***, 2117-2120 (1951).
37. Rebsdat, S., Ethylene Glycol. In *Ullmann's Encyclopedia of Industrial Chemistry*, 7 ed.; Wiley-VCH, Weinheim (2000).

38. Rice, S. A.; Kenney-Wallace, G. A., Time-resolved fluorescence depolarization studies of rotational relaxation in viscous media. *Chem. Phys.* ***47***, 161-170 (1980).
39. Shirota, H.; Funston, A. M.; Wishart, J. F.; Jr., E. W. C., Ultrafast dynamics of pyrrolidinium cation ionic liquids. *J. Chem. Phys.* ***122***, 184512 (2005).
40. Karmakar, R.; Samanta, A., Dynamics of Solvation of the Fluorescent State of Some Electron Donor,àíAcceptor Molecules in Room Temperature Ionic Liquids, [BMIM][(CF3SO2)2N] and [EMIM][(CF3SO2)2N]. *J Phy Chem A* ***107***, 7340-7346 (2003).
41. Pramanik, R.; Rao, V. G.; Sarkar, S.; Ghatak, C.; Setua, P.; Sarkar, N., To Probe the Interaction of Methanol and Acetonitrile with the Ionic Liquid N,N,N-Trimethyl-N-propyl Ammonium Bis(trifluoromethanesulfonyl) Imide at Different Temperatures by Solvation Dynamics Study. *J. Phys. Chem. B* ***113***, 8626-8634 (2009).
42. Wiseman, T.; Williston, S.; Brandts, J. F.; Lin, L.-N., Rapid measurement of binding constants and heats of binding using a new titration calorimeter. *Anal. Biochem.* ***179***, 131-137 (1989).
43. Jelesarov, I.; Bosshard, H. R., Isothermal titration calorimetry and differential scanning calorimetry as complementary tools to investigate the energetics of biomolecular recognition. *J. Mol. Recognit.* ***12***, 3-18 (1999).
44. Leavitt, S.; Freire, E., Direct measurement of protein binding energetics by isothermal titration calorimetry. *Curr. Opin. Struc. Biol.* ***11***, 560-566 (2001).
45. Lindman, S.; Lynch, I.; Thulin, E.; Nilsson, H.; Dawson, K. A.; Linse, S., Systematic Investigation of the Thermodynamics of HSA Adsorption to N-iso-Propylacrylamide/N-tert-Butylacrylamide Copolymer Nanoparticles. Effects of Particle Size and Hydrophobicity. *Nano Lett.* ***7***, 914-920 (2007).
46. Varghese, N.; Mogera, U.; Govindaraj, A.; Das, A.; Maiti, P. K.; Sood, A. K.; Rao, C. N. R., Binding of DNA Nucleobases and Nucleosides with Graphene. *ChemPhysChem* ***10***, 206-210 (2009).
47. Todd, M. J.; Gomez, J., Enzyme Kinetics Determined Using Calorimetry: A General Assay for Enzyme Activity? *Anal. Biochem.* ***296***, 179-187 (2001).
48. Le Berre, M.; Chen, Y.; Baigl, D., From Convective Assembly to Landau−Levich Deposition of Multilayered Phospholipid Films of Controlled Thickness. *Langmuir* ***25***, 2554-2557 (2009).
49. Kwok, D. Y.; Neumann, A. W., Contact angle measurement and contact angle interpretation. *Adv. Colloid Interface Sci.* ***81***, 167-249 (1999).
50. Young, T., III. An essay on the cohesion of fluids. *Philos. Trans. Royal Soc.* ***95***, 65-87 (1805).
51. Schneider, C. A.; Rasband, W. S.; Eliceiri, K. W., NIH Image to ImageJ: 25 years of image analysis. *Nat. Methods* ***9***, 671 (2012).
52. Köhler, A.; dos Santos, D. A.; Beljonne, D.; Shuai, Z.; Brédas, J. L.; Holmes, A. B.; Kraus, A.; Müllen, K.; Friend, R. H., Charge Separation in Localized and Delocalized Electronic States in Polymeric Semiconductors. *Nature* ***392***, 903 (1998).
53. Comoretto, D.; Dellepiane, G.; Marabelli, F.; Cornil, J.; dos Santos, D. A.; Bredas, J. L.; Moses, D., Optical Constants of Highly Stretch-Oriented Poly(P-Phenylene-Vinylene): A Joint Experimental and Theoretical Study. *Phys. Rev. B: Condens. Matter Mater. Phys.* ***62***, 10173 (2000).
54. Gather, M. C.; Bradley, D. D. C., An Improved Optical Method for Determining the Order Parameter in Thin Oriented Molecular Films and Demonstration of a Highly Axial Dipole Moment for the Lowest Energy pi–pi* Optical Transition in Poly(9,9- Dioctylfluorene-Co-Bithiophene). *Adv. Funct. Mater.* ***17***, 479 (2007).

55. Vezie, M. S.; Few, S.; Meager, I.; Pieridou, G.; Dorling, B.; Ashraf, R. S.; Goni, A. R.; Bronstein, H.; McCulloch, I.; Hayes, S. C.; Campoy-Quiles, M.; Nelson, J., Exploring the Origin of High Optical Absorption in Conjugated Polymers. *Nat. Mater.* ***15***, 746 (2016).
56. Baker, J. L.; Jimison, L. H.; Mannsfeld, S.; Volkman, S.; Yin, S.; Subramanian, V.; Salleo, A.; Alivisatos, A. P.; Toney, M. F., Quantification of thin film crystallographic orientation using X-ray diffraction with an area detector. *Langmuir* ***26***, 9146-9151 (2010).
57. Jiang, Z.; Li, X.; Strzalka, J.; Sprung, M.; Sun, T.; Sandy, A. R.; Narayanan, S.; Lee, D. R.; Wang, J., The dedicated high-resolution grazing-incidence X-ray scattering beamline 8-ID-E at the Advanced Photon Source. *J. Synchrotron Rad.* ***19***, 627-636 (2012).
58. Jiang, Z., GIXSGUI: a MATLAB toolbox for grazing-incidence X-ray scattering data visualization and reduction, and indexing of buried three-dimensional periodic nanostructured films. *J. Appl. Cryst.* ***48***, 917-926 (2015).
59. Ito, Y.; Virkar, A. A.; Mannsfeld, S.; Oh, J. H.; Toney, M.; Locklin, J.; Bao, Z., Crystalline Ultrasmooth Self-Assembled Monolayers of Alkylsilanes for Organic Field-Effect Transistors. *J. Am. Chem. Soc.* ***131***, 9396-9404 (2009).

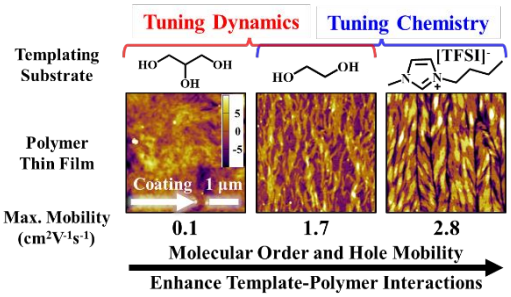

Substrate-conjugated polymer interaction strength serves as a unifying metric to gauge the effectiveness of dynamic templates in directing crystallization.